

# Structure development of resorcinol-formaldehyde gels: Microphase separation or colloid aggregation

Cedric J. Gommès<sup>1</sup> and Anthony P. Roberts<sup>2</sup>

<sup>1</sup>*Department of Chemical Engineering, University of Liège B6a, Allée du 6 août 3, B-4000 Liège, Belgium*

<sup>2</sup>*Department of Mathematics, University of Queensland, Brisbane, Queensland 4072, Australia*

(Received 22 January 2008; published 23 April 2008)

Time-resolved small-angle x-ray scattering (SAXS) is used to follow the formation of resorcinol-formaldehyde (RF) gels. An existing morphological model based on Gaussian random fields, and validated on RF aerogels, is generalized to analyze the data. The generalization is done in two different ways, one being relevant to colloid aggregation and the other to microphase separation. The SAXS data do not enable discrimination between the two mechanisms of gel formation, which shows that aggregation and microphase separation can generate very similar morphologies at the length scales explored by SAXS. Furthermore, physical arguments suggest that, in the case of RF gels, aggregation and microphase separation can be regarded as two idealizations of the same complex physical process.

DOI: [10.1103/PhysRevE.77.041409](https://doi.org/10.1103/PhysRevE.77.041409)

PACS number(s): 82.70.Gg, 61.05.cf, 61.43.Bn

## I. INTRODUCTION

Chemical gels are obtained from the polymerization of precursor molecules in a solvent, until the obtained macromolecules form a network that percolates through the solution. In some cases, the macromolecules and the solvent are mixed at a molecular scale, in which case the gel is made of a single phase that is locally not different from a solution [1]. In many instances, however, the gel is biphasic as it is made of a solid polymer skeleton and of a liquid phase, both having very complex morphologies with a characteristic size in the nanometer range. The latter gels are sometimes referred to as being colloidal and the former as being polymeric. Colloidal gels are of a particular importance in materials science as they are an intermediate step in the sol-gel synthesis of nanostructured materials [2]. Therefore, understanding the physical and chemical mechanisms that control the structuring of colloidal gels is of both fundamental and practical importance.

Researchers active in different disciplines use different paradigms to explain the processes that govern the formation of colloidal gels. The formation of inorganic gels—like SiO<sub>2</sub> [3], TiO<sub>2</sub> [4], or ZrO<sub>2</sub> [5]—from the polycondensation of alkoxide precursors is often discussed in terms of the aggregation of colloidal particles. According to this scenario, the precursor molecules polymerize to form first dense colloidal particles that afterward aggregate to form a space-filling cluster. This scenario was made very popular in the 1980s and 1990s through the use of fractal concepts, like diffusion-limited aggregation (DLA) or reaction-limited aggregation (RLA) [6,7]. This scenario is supported by the microscopy observation of the gels after desiccation; their structure can be thought of as filamentary aggregates of colloidal particles, which are sometimes referred to as strings of pearls. For many systems, *in situ* small-angle x-ray scattering (SAXS) data can be analyzed in the frame of an aggregation model, e.g., [8,9].

When analyzing the structuring of organic colloidal gels, on the other hand, fractal concepts are rarely used: the process that is most often hypothesized is microphase separation [10–12]. According to this process, the polymerization first

leads to a polymeric gel or microgel; the progressive increase of the reticulation of the network is accompanied by a lowering of the solubility of the polymer, which triggers a demixing process. During the demixing, the existing polymer folds up so as to create a dense skeleton, the pores of which are filled with pure solvent. There are theoretical arguments showing that the occurrence of microphase separation in gelling systems leads to a spongelike morphology [13] that is very similar to the string-of-pearls morphology of many inorganic gels.

Resorcinol-formaldehyde gels [14,15] are materials that are of interest to both researchers active in the domain of organic polymers and researchers active in the sol-gel synthesis of porous materials, who often have a background in inorganic chemistry. Accordingly, the formation of the microstructure of that particular type of material is sometimes analyzed in terms of a microphase separation [16], and sometimes in terms of an aggregation process [17].

In the present paper, *in situ* small-angle x-ray scattering is used to analyze the development of the morphology of resorcinol-formaldehyde (RF) gels synthesized in alkaline conditions. The morphology of the final gels is well described by a geometrical model based on the level cut of Gaussian random fields [18]. This model is generalized in two independent ways, so as to analyze the SAXS data in terms of an aggregation process on one hand, and of a microphase separation on the other hand. The results of the two different analyses of the same data set give some insight into the structure development of RF gels and help reconcile the two apparently opposing conceptions.

## II. EXPERIMENTAL SECTION

### A. Preparation of the gels

Organic aqueous gels were produced from polycondensation of resorcinol and formaldehyde in water with sodium carbonate as a catalyst, as described thoroughly elsewhere [19]. The resorcinol/formaldehyde molar ratio was set to  $R/F=0.5$ , the dilution molar ratio  $D=\text{water}/(\text{resorcinol}$

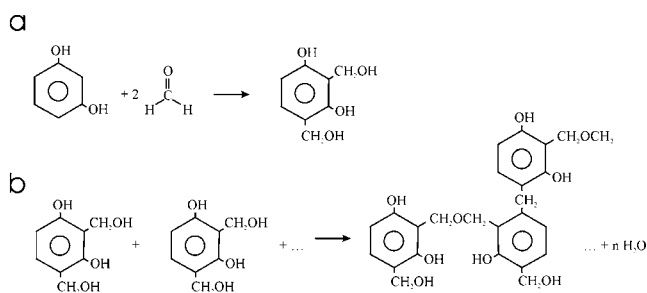


FIG. 1. Main reactions involved in the gel formation from resorcinol and formaldehyde: (a) addition reactions and (b) condensation reactions with water being released.

+formaldehyde+sodium carbonate) was set to 6, and six gels were analyzed corresponding to resorcinol/sodium carbonate molar ratios equal to  $R/C=1000, 250, 200, 150, 100,$  and 50. After dissolution of resorcinol (Vel, 99%) and sodium carbonate (UCB, 99.5%) in deionized water under stirring, formaldehyde (Aldrich, 37 wt % in water, stabilized by 10–15 wt % methanol) was added.

The major reactions implied in the formation of the gels are sketched in Fig. 1 (see, e.g., [15]), both of which are base catalyzed. Hydroxymethyl groups ( $-\text{CH}_2\text{OH}$ ) are added to the resorcinol ring via an addition reaction [Fig. 1(a)]. Subsequent condensation reactions occur by which resorcinol rings link together to form a three-dimensional gel-forming network [Fig. 1(b)]. The links between resorcinol rings can result either from the condensation of two hydroxymethyl groups or from the condensation of a hydroxymethyl with a hydroxyl group; both reactions release water.

The density of the solid forming the skeleton of the gel, measured by helium pycnometry after drying, is about  $1.5 \text{ g/cm}^3$  [19]. With that value, and from the composition of the reacting solutions reported earlier, the volume fraction of the gel that is indeed occupied by its solid skeleton is estimated to be 23%.

## B. SAXS measurements and raw data

The time-resolved SAXS measurements were done at DUBBLE, the Dutch-Flemish beamline BM26 at the Euro-

pean Synchrotron Radiation Facility (Grenoble, France). Immediately after the preparation of the gel-forming solution, a small fraction of it is extracted from the flask and placed in a 1.5-mm-thick cell with parallel mica windows, with the temperature set to  $70^\circ\text{C}$ . Consecutive *in situ* pinhole SAXS patterns are recorded over time spans of 30 s on a two-dimensional (2D) charge-coupled device (CCD) detector placed at 3.5 m from the sample. At  $70^\circ\text{C}$ , the gelation of the solutions occurs in about 60 min in the flask and after 30 min in the measuring cell, which points to an effect of x-ray irradiation on the gel-forming reactions.

The SAXS intensity is expressed as a function of the scattering vector modulus  $q=(4\pi/\lambda)\sin(\theta/2)$ ,  $\lambda$  being the wavelength (set to  $1 \text{ \AA}$ ) and  $\theta$  the scattering angle. The intensity scattered by the empty sample holder is measured and subtracted from the scattering patterns. A correction is made for the detector response, and the data are normalized to the intensity of the primary beam measured by an ionization chamber placed downstream from the sample. The number of counts in the patterns at the high- $q$  limit of the SAXS is about one order of magnitude larger for the samples than for the empty cell.

The SAXS patterns  $I(q, t)$  measured during the formation of the gels are reported in Fig. 2 on double logarithmic scales. Globally, the intensity scattered by any sample increases with reaction time; at any given reaction time  $I(q)$  exhibits a plateau at small angles and decreases with  $q$  at larger angles. Toward the end of the runs, the decrease of  $I$  with increasing  $q$  at large angles follows roughly a power law with exponent 4 (Porod's scattering). For small reaction times, however, the decrease of  $I$  vs  $q$  is less steep.

Three trends are visible when the gels are prepared with smaller and smaller  $R/C$  ratios. First, the evolution of the SAXS patterns becomes more rapid [see e.g., Fig. 2(f) compared to Fig. 2(a)]. Second, the cutoff between the plateau and the Porod scattering region moves toward larger scattering angles, which points to smaller structures. Third, a slight maximum appears in the patterns that points to a structure with a better-defined characteristic length.

The SAXS patterns for  $q > 0.1 \text{ \AA}^{-1}$  are first fitted with the following equation:

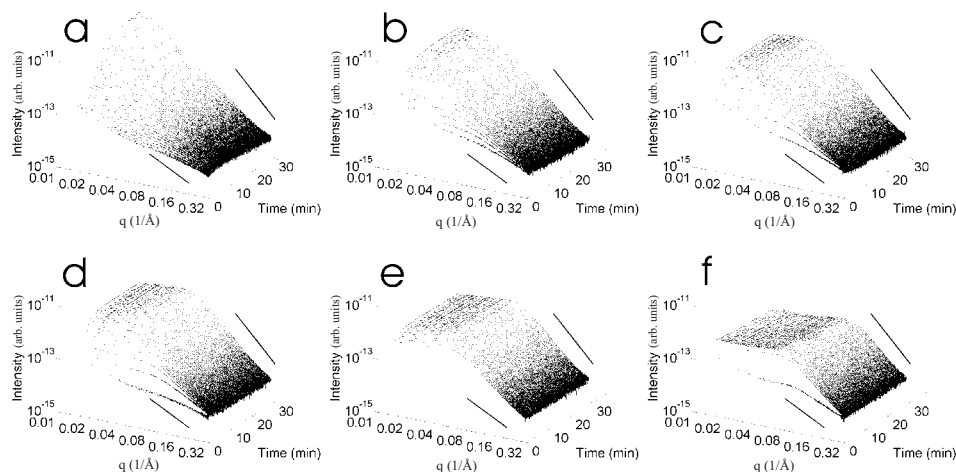


FIG. 2. Time-resolved SAXS patterns measured during the formation of resorcinol-formaldehyde gels with  $R/C=1000$  (a), 250 (b), 200 (c), 150 (d), 100 (e), and 50 (f). The two straight lines added to each graph are power law scatterings of the type  $I \sim q^{-2}$  ( $t=0$  min) and  $I \sim q^{-4}$  ( $t=30$  min).

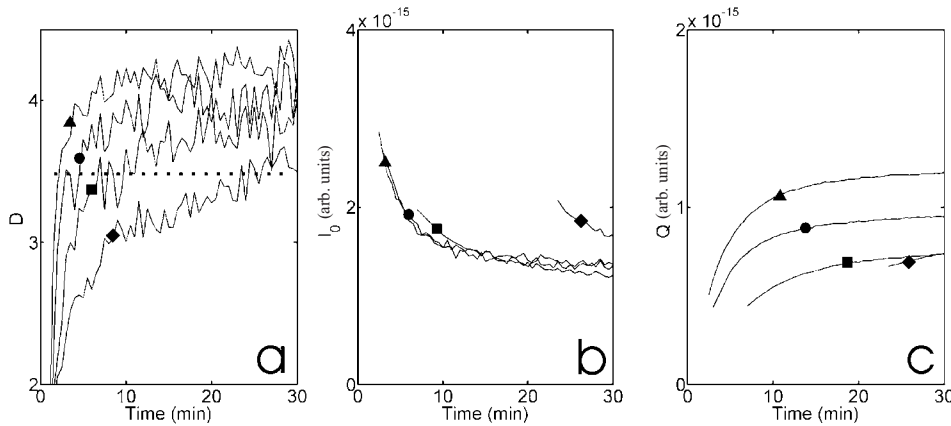


FIG. 3. Temporal evolution of the asymptotic scattering exponent  $D$  (a), of the background scattering  $I_0$  (b), and of Porod's invariant  $Q$  (c), during the formation of gels with  $R/C=1000$  ( $\blacklozenge$ ), 250 ( $\blacksquare$ ), 200 ( $\bullet$ ), and 150 ( $\blacktriangle$ ). The dotted horizontal line in (a) corresponds to  $D=3.5$ , below which value  $I_0$  and  $Q$  are not estimated (see text).

$$I(q) = Aq^{-D} + I_0 \quad (1)$$

with  $A$ ,  $D$ , and  $I_0$  as adjustable parameters, with the only aim of estimating roughly the asymptotic exponent  $D$ . The evolution of  $D$  with time is plotted in Fig. 3(a); for all gels  $D$  is initially close to 2 and it progressively increases until a value close to 4 is reached. Due mostly to numerical correlations between the various parameters in Eq. (1), the value of  $D$  cannot be estimated very precisely [Fig. 3(a)]. Therefore, whenever  $D > 3.5$ , its value was set to  $D=4$ , and Eq. (1) was fitted again to the data with  $A$  and  $I_0$  as the only adjustable parameters. The obtained values of  $I_0$  are plotted in Fig. 3(b); the background scattered intensity  $I_0$  is seen to decrease with reaction time.

With the estimated value of  $I_0$ , the total scattered intensity (Porod's invariant) is estimated as [20]

$$Q = \int_0^\infty [I(q) - I_0] 4\pi q^2 dq, \quad (2)$$

where the integration outside the measured  $q$  range is done by extrapolating  $I(q) - I_0$  as  $Aq^{-4}$ , in agreement with Eq. (1), and  $D=4$ . The temporal evolution of  $Q$  is plotted in Fig. 3(c); for all gels  $Q$  increases continuously with reaction time until a plateau is reached at intermediate reaction times. Note that the estimation of  $Q$  is justified only when a Porod scattering is observed, which we considered to be the reaction times with  $D > 3.5$  in Fig. 3(a).

### III. MODEL OF THE GEL'S MORPHOLOGY AND ANALYSIS OF THE SAXS DATA

Two important features of the SAXS data presented in Figs. 2 and 3 are (i) the existence of a Porod scattering region with exponent 4, which—as nicely put by Ciccariello *et al.* [21]—“ensures that the sample admits an idealization with sharp boundaries,” and (ii) the presence of background scattering at large angles, which points to the presence of a structure with a characteristic size smaller than the resolution limit of the SAXS. The background scattering  $I_0$  decreases with reaction time, which indicates the disappearance of the corresponding small-scale structure. Over the same period the total intensity  $Q$  scattered by the large-scale structure progressively increases, implying a change of electron den-

sity contrast or of the volume fraction of the phases [20].

Figure 4 shows two different models that could qualitatively explain the evolution of the SAXS data. In model A [Fig. 4(a)], the skeleton of the gel is uniform, with electron density  $\rho_P$  corresponding to the dense polymer, and the liquid filling the pores of the gel is a colloidal suspension of polymer particles of density  $\rho_L$  in a pure liquid of electron density  $\rho_L$ . Another possible morphological model [model B, Fig. 4(b)] is a uniform liquid phase, with density  $\rho_L$ , filling the largest pores of a skeleton, the skeleton also having much smaller pores, also filled with liquid. When discussing model B, we shall comply with the recommendations of the International Union of Pure and Applied Chemistry and refer to the largest pores of the skeleton as *mesopores*, and to the smallest pores within the skeleton as *micropores* [22].

In the course of the gel formation, the morphology and the volume fractions of the various phases possibly evolve; the model used to analyze the SAXS data must therefore incorporate both the small-scale and the large-scale structures, as well as ensure polymer conservation in the gel-forming process. In Sec. III A, a general expression is derived for the scattering by a biphasic structure with two very different length scales. This expression is afterwards specialized and used to analyze the time-resolved SAXS data.

#### A. Scattering by a biphasic structure with two very different length scales

The intensity scattered by a statistically isotropic system is proportional to the Fourier transform of the autocorrelation

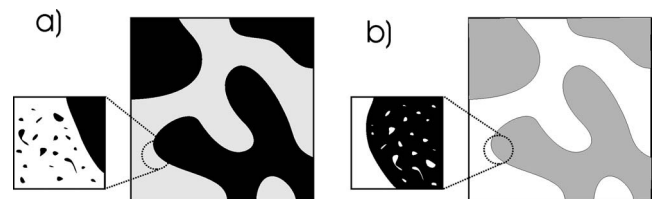


FIG. 4. Sketch of the two different two-scale models of the gel used to analyze the SAXS data. In model A, the solid skeleton of the gel is a dense polymer, while the liquid phase is a colloidal suspension. In model B, the liquid phase is pure solvent, while the solid skeleton comprises small pores filled with solvent. In both cases, the characteristic length of the large-scale structure is assumed *a priori* to be much larger than that of the small-scale structure.

function of the electron density  $\rho(x)$  of the system, i.e., [20]

$$\frac{I(q)}{I_e V} = \int_0^\infty [\langle \rho(x+r)\rho(x) \rangle - \langle \rho(x) \rangle^2] \frac{\sin(qr)}{qr} 4\pi r^2 dr, \quad (3)$$

where the  $\langle \rangle$  is the average over all possible values of  $x$ ,  $I_e$  is the intensity scattered by a single electron, and  $V$  is the irradiated volume. The purpose of the present section is to derive a general expression for the intensity scattered by a two-scale model as sketched in Fig. 4. For the sake of clarity we shall derive the expression in the case of model A, its generalization to model B being straightforward.

Let  $\Phi_S(x)$  be the indicator function of the skeleton, i.e.,  $\Phi_S(x)$  takes the value 1 in the skeleton and 0 in the pore space [23]. Similarly, let  $\Phi_C(x)$  be the indicator function of colloidal polymer suspension that fills the pores of the skeleton;  $\Phi_C(x)$  is defined as if that phase filled the entire space and is not confined to the pores of the gel's skeleton. With these notations, the electron density can be written as

$$\rho(x) = \rho_P \Phi_S(x) + [1 - \Phi_S(x)]\{\rho_L[1 - \Phi_C(x)] + \rho_P \Phi_C(x)\}, \quad (4)$$

where  $\rho_P$  is the electron density of the polymer making both skeleton and colloidal phase, and  $\rho_L$  is the electron density of the liquid. From Eq. (4), the average electron density is

$$\langle \rho \rangle = [\phi_S + (1 - \phi_S)\phi_C]\rho_P + [1 - \phi_S - (1 - \phi_S)\phi_C]\rho_L, \quad (5)$$

where  $\phi_S = \langle \Phi_S \rangle$  ( $\phi_C = \langle \Phi_C \rangle$ ) is the volume fraction of the skeleton (colloidal polymer); in Eq. (5) it has been assumed that the random processes  $S$  and  $C$  are statistically independent, which implies  $\langle \Phi_C(x)\Phi_S(x) \rangle = \langle \Phi_C(x) \rangle \langle \Phi_S(x) \rangle$ . Similarly, from Eqs. (4) and (5), one finds

$$\begin{aligned} & \langle \rho(x+r)\rho(x) \rangle - \langle \rho(x) \rangle^2 \\ &= (\Delta\rho)^2 \{ (1 - \phi_C)^2 [P_{SS}(r) - \phi_S^2] + (1 - \phi_S)^2 [P_{CC}(r) - \phi_C^2] \\ & \quad + [P_{SS}(r) - \phi_S^2][P_{CC}(r) - \phi_C^2] \}, \end{aligned} \quad (6)$$

where  $\Delta\rho = \rho_P - \rho_L$  is the electron density contrast between the polymer and the liquid, and where the notation

$$P_{SS}(r) = \langle \Phi_S(x+r)\Phi_S(x) \rangle \quad (7)$$

was used for the two-point probability function of the skeleton. Similarly,  $P_{CC}(r)$  is the two-point probability function of the colloidal polymer suspension, in the absence of the skeleton.

The two-point probability function  $P_{CC}(r)$  is the probability that two points at a distance  $r$  from each other, taken randomly in the system, both belong to phase  $C$  (see, e.g., [23–25]). For  $r=0$ , i.e., if the two points coincide,  $P_{CC} = \phi_C$ , and  $P_{CC}$  converges to  $\phi_C^2$  for large values of  $r$ . The decrease of  $P_{CC}(r)$  from  $\phi_C$  to  $\phi_C^2$  occurs over a distance  $r$  that compares with the characteristic size  $L_C$  of  $C$ . The same applies *mutatis mutandis* to  $P_{SS}$ . Therefore, the term  $[P_{SS}(r) - \phi_S^2][P_{CC}(r) - \phi_C^2]$  in Eq. (6) is significantly different from zero only for values of  $r$  smaller than  $L_C$ . As the characteristic length of  $S$  is, by assumption, much larger than  $L_C$ , one can approximate  $P_{SS}(r) \approx \phi_S$ . This implies

$$[P_{SS}(r) - \phi_S^2][P_{CC}(r) - \phi_C^2] \approx \phi_S(1 - \phi_S)[P_{CC}(r) - \phi_C^2]. \quad (8)$$

Using Eqs. (6), the scattered intensity is estimated from Eq. (3) to be

$$\frac{I^A(q)}{I_e V} = [(1 - \phi_C)\Delta\rho]^2 I_S(q) + (1 - \phi_S)(\Delta\rho)^2 I_C(q) \quad (9)$$

with

$$I_S(q) = \int_0^\infty [P_{SS}(r) - \phi_S^2] \frac{\sin(qr)}{qr} 4\pi r^2 dr, \quad (10)$$

and a similar definition for  $I_C(q)$ . Equation (9) shows that the small-angle scattering by a structure having the morphology of Fig. 4(a) (model A) is the sum of two contributions. One contribution is the scattering from the skeleton, with electron density  $\rho_P$ , the pores of which are filled with a liquid of average electron density  $\rho_L + \Delta\rho\phi_C$ , so that the effective contrast between the two phases is  $(1 - \phi_C)\Delta\rho$ . The second contribution is the scattering from the colloidal polymer suspension, the contrast of which with the liquid is simply  $\Delta\rho$ . This contribution is, however, weighted by the factor  $(1 - \phi_S)$ , because this is the fraction of the total irradiated volume that is occupied by that structure.

The case of model B [Fig. 4(b)] is handled in the same way; instead of Eq. (9), one finds

$$\frac{I^B(q)}{I_e V} = [(1 - \phi_{MP})\Delta\rho]^2 I_S(q) + \phi_S(\Delta\rho)^2 I_{MP}(q) \quad (11)$$

where  $I_{MP}(q)$  is defined by a relation identical to Eq. (10).  $\phi_{MP}$  is the volume fraction of the micropores within the skeleton; it should not be confused with the fraction of micropores in the whole sample, which is given by  $\phi_S\phi_{MP}$ .

## B. Specific large-scale and small-scale models

Equations (9) and (11) are very general. In this section, they are specialized with the aim of analyzing the *in situ* SAXS data collected during resorcinol-formaldehyde gel formation. The SAXS patterns [Sec. II B and Fig. 3(b)] have a background scattering, which we attribute to the small-scale structure. Let us first focus on model A.

As the colloidal phase gives rise to a background scattering uniform over all measured angles, it is natural—in the frame of model A—to model it as a dilute suspension of objects with a size smaller than the resolution limit of the SAXS. In such a case (see, e.g., [20,26]), the intensity scattered by the small-scale structure depends only on the concentration  $c$  of the dispersed objects and on their average volume  $v$  through

$$I_C(q) \approx cv^2, \quad (12)$$

which, from Eq. (9), predicts a background scattering of intensity

$$I_0^A = I_e V (\Delta\rho)^2 (1 - \phi_S)\phi_C v, \quad (13)$$

where it has been taken into account that  $\phi_C = cv$ .

The derivation of Eq. (12) is based on the general assumption that the structure is made of objects of volume  $v$  that scatter incoherently from one another [20]. Equation (12) is therefore not restricted to diluted suspensions; it applies to any system of noninteracting objects. If the micropore structure (model B) is modeled as a Poisson process [23,27], i.e., as a random distribution of possibly overlapping pores, Eq. (12) applies, with  $v$  the volume of the micropores and  $c$  their concentration. In such a case, the background scattering is

$$I_0^B = I_e V (\Delta\rho)^2 \phi_S \phi_{MP} v, \quad (14)$$

which is the equivalent of Eq. (13) in the case of model B.

In the case of resorcinol-formaldehyde aerogels, i.e., after supercritical removal of the solvent (see, e.g., [2]), the morphology of the gel's skeleton is well described by the Gaussian random field intersection model of Roberts [18]. The model is described in detail in the Appendix. Briefly, two statistically independent Gaussian random fields (GRFs)  $y(\mathbf{x})$  and  $w(\mathbf{x})$  are considered, with mean equal to zero and variance equal to one. Given two thresholds  $\alpha$  and  $\beta$ , the solid skeleton of the gel is defined as the regions of space where both  $\alpha \leq y(x) \leq \beta$  and  $\alpha \leq w(x) \leq \beta$ . The following functional form is chosen for the field-field correlation function of the GRFs:

$$g(r) = \frac{1}{\cosh(r/\xi)} \frac{\sin(2\pi r/d)}{(2\pi r/d)}. \quad (15)$$

This analytical form is simpler than the one used in Ref. [18]; it has only two parameters: a correlation length  $\xi$  and a domain scale  $d$ . The correlation length  $\xi$  can be thought of as the size of the uniform regions (either positive or negative) in the GRFs, and the  $d$ -dependent factor in Eq. (15) introduces a short-range order in the structure, which is responsible for the presence of a peak in the scattering patterns.

As discussed in more detail in the Appendix, the field-field correlation function in Eq. (15) is quadratic for vanishingly small values or  $r$ , which guarantees that the specific surface area of the level-cut morphology is finite. The scattering function  $I_S(q)$ , to be used in Eq. (9) or Eq. (11), is calculated numerically through Eq. (10) using the two-point probability function of the intersection model given in the Appendix [Eqs. (A7) and (A9)].

### C. Analysis of the SAXS data

At any reaction time,  $I_0$  and  $Q$  are determined from Eqs. (1) and (2), and the SAXS data are fitted by least-squares minimization to

$$\frac{I(q) - I_0}{Q} = \frac{1}{(2\pi)^3} \frac{I_S(q)}{\phi_S(1 - \phi_S)}, \quad (16)$$

which results from Eqs. (9) and (13) for model A [Eqs. (11) and (14) for model B], and where we have taken account of the general result [20]

$$\int_0^\infty I_S(q) 4\pi q^2 dq = (2\pi)^3 \phi_S(1 - \phi_S) \quad (17)$$

that applies to any biphasic structure. The parameters that enter the right-hand side of Eq. (16) are the two characteristic lengths of the GRFs  $\xi$  and  $d$ , and the two thresholds  $\alpha$  and  $\beta$ . Note that  $\phi_S$  is related to  $\alpha$  and  $\beta$  via Eq. (A8) of the Appendix.

It will hereafter be assumed that the development of the gel's morphology is finished at the end of the measurements, i.e., that the skeleton is made of dense polymer, and its pores are filled with pure solvent. In the frame of the two models of Fig. 4, this is equivalent to assuming  $\phi_C=0$  (model A), or  $\phi_{MP}=0$  (model B) at the end of the measurement. In this case, the two models are identical to the model used by Roberts to analyze the structure of aerogels [18]. Polymer conservation implies  $\phi_S = \phi_S^\infty = 0.23$  at the end of the runs (Sec. II B). Using this value of  $\phi_S$  in Eq. (16), the SAXS patterns are fitted with only three adjustable parameters:  $\xi$ ,  $d$ , and one single threshold  $\beta$ . Figure 5(a) compares the data with the fitted model. The gel with  $R/C=1000$  is not analyzed because its SAXS pattern at the end of the measurement [Fig. 2(a)] exhibits only Porod scattering, which points to structures larger than the upper resolution of the SAXS. Figure 6 shows realizations of the intersection model with the fitted parameters corresponding to gels with various  $R/C$  ratios. The discussion of this figure is postponed to Sec. IV.

To analyze the SAXS patterns at any intermediate reaction time, the value of the total intensity  $Q$  [Fig. 3(c)] is first used to estimate the volume fraction of the skeleton at that particular time. For model A, from Eqs. (2), (9), and (12), one finds

$$Q = (2\pi)^3 I_e V (\Delta\rho)^2 (1 - \phi_C)^2 \phi_S(1 - \phi_S), \quad (18)$$

where Eq. (17) was used. The unknown quantities  $I_e$  and  $V$  are constant in time; they can therefore be removed from Eq. (18) by considering the ratio of  $Q$  to its final value  $Q^\infty$ , corresponding to  $\phi_C=0$  and  $\phi_S^\infty=0.23$ . Furthermore, at any stage of the gel formation, polymer volume conservation implies the following relation between  $\phi_S$  and  $\phi_C$ :

$$\phi_S + (1 - \phi_S)\phi_C = \phi_S^\infty. \quad (19)$$

Combining Eqs. (18) and (19) leads to the following estimate of  $\phi_S$ :

$$\phi_S^A = \left( 1 + \frac{1 - \phi_S^\infty Q^\infty}{\phi_S^\infty Q} \right)^{-1}, \quad (20)$$

where the exponent  $A$  highlights the fact that this expression is valid for model A only. An estimate of the volume of the objects in the dispersed colloidal polymer phase can be obtained by combining Eqs. (13), (18), and (19), giving

$$v^A = (2\pi)^3 \frac{I_0}{Q} \frac{\phi_S}{1 - \phi_S} \frac{(1 - \phi_S^\infty)^2}{\phi_S^\infty - \phi_S}. \quad (21)$$

Figures 7(a1)–7(c1) plot the time evolution of the volume fractions  $\phi_S$  and  $\phi_C$ , as well as the volume of the colloids  $v$ . The evolution of  $\phi_C$  and  $v$  is roughly exponential [note the semilogarithmic axes in Figs. 7(b1) and 7(c1)].

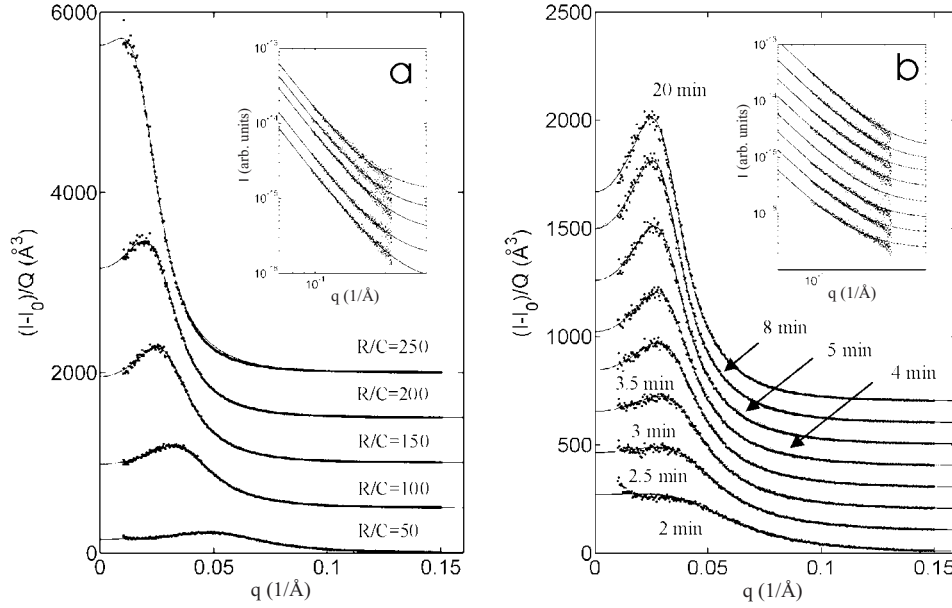


FIG. 5. Example fits of the intersection model to the final SAXS patterns of gels with various  $R/C$  ratios (a), and to the intermediate SAXS patterns of the gel with  $R/C=150$  (b). In (b), the solid and dotted lines are the best fits with models A and B, respectively (the two models are nearly indistinguishable). The insets show on a double-logarithmic scale the intensities scattered at large angle, as well as their fit with Eq. (1) with  $D=4$ . The curves are arbitrarily shifted vertically and the order of the curves is the same in the insets and in the main figures.

Once the volume fraction of the skeleton is known from Eq. (20), the value is used in Eq. (16) to fit the SAXS data with the intersection model, with  $\xi$ ,  $d$ , and  $\beta$  as the only adjustable parameters. The quality of the fits is illustrated in Fig. 5(b). Instead of plotting  $\xi$  and  $d$  independently, it is convenient to visualize the evolution of the specific surface area of the skeleton  $S$ , obtained from Eq. (A12) of the Appendix. Furthermore, as the volume fraction of the skeleton is changing with reaction time, it is useful to consider the ratio  $S/\phi_S$ , which is inversely proportional to the average chord length of the skeleton [23,28]. As seen in Fig. 8(a1),  $S/\phi_S$  decreases with reaction time, which points to a coarsening of the skeleton. Another parameter of interest is the ratio  $\xi/d$ , which is related to the presence of a peak in the scattering patterns [18] and can therefore be thought of as a measure of the regularity of the structure (see the Appendix). For all gels,  $\xi/d$  increases at early reaction time and remains constant afterward [Fig. 8(b1)]. The evolution of the upper threshold  $\beta$  used to define the level-cut Gaussian field is plotted in Fig. 8(c1).

The results presented so far [Figs. 7(a1)–7(c1) and 8(a1)–8(c1)] are for model A. A similar analysis can be carried out for model B. For model B, polymer conservation implies

$$\phi_S(1 - \phi_{MP}) = \phi_S^\infty. \quad (22)$$

The same analysis as the one leading to Eq. (20) leads to

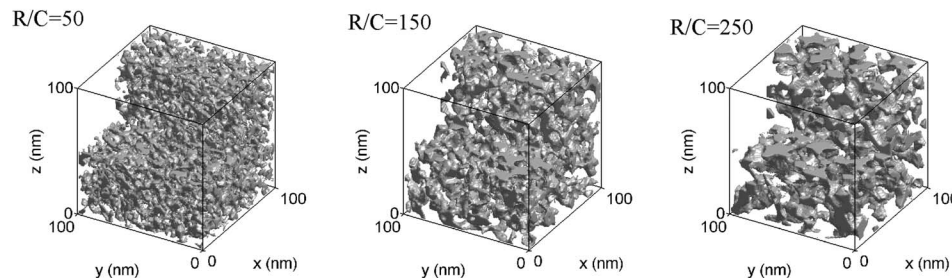


FIG. 6. Realizations of the intersection model with the parameters corresponding to the optimal fits of the SAXS patterns of the final gels:  $d=112$  Å,  $\xi=36$  Å,  $\beta=-0.04$  ( $R/C=50$ );  $d=210$  Å,  $\xi=63$  Å,  $\beta=-0.02$  ( $R/C=150$ );  $d=340$  Å,  $\xi=67$  Å,  $\beta=-0.02$  ( $R/C=250$ ); for all gels  $\phi_S=0.23$ .

$$\phi_S^B = \left( 1 + \frac{1 - \phi_S^\infty}{\phi_S^\infty} \frac{Q}{Q^\infty} \right)^{-1} \quad (23)$$

in the case of model B, and the volume of the micropores is obtained as

$$v^B = (2\pi)^3 \frac{I_0}{Q} \frac{1 - \phi_S}{\phi_S} \frac{(\phi_S^\infty)^2}{\phi_S - \phi_S^\infty}, \quad (24)$$

which is analogous to Eq. (21). The evolution of  $\phi_S$ ,  $\phi_{MP}$ , and  $v$  in the case of model B is plotted in Figs. 7(a2)–7(c2). The evolution of  $Q$  and  $I_0$  is interpreted in the framework of model B as shrinkage of the skeleton [Fig. 7(a2)] resulting from the progressive disappearance of its microporosity [Fig. 7(b2)], the volume of the micropores [Fig. 7(c2)] increasing exponentially with time (this is discussed below). On the basis of the estimated volume fraction  $\phi_S$ , the SAXS data are also fitted with Eq. (16) [Fig. 5(b)]. The corresponding values of  $S/(1 - \phi_S)$ ,  $\xi/d$ , and  $\beta$  are plotted in Figs. 8(a2)–8(c2). Note that the ratio  $S/(1 - \phi_S)$  is inversely proportional to the average chord length of the mesopores.

#### IV. DISCUSSION

The two main hypotheses that underlie the used modeling methodology are (i) that the structure of the gels is biphasic comprising a polymer phase and a liquid phase, with conser-

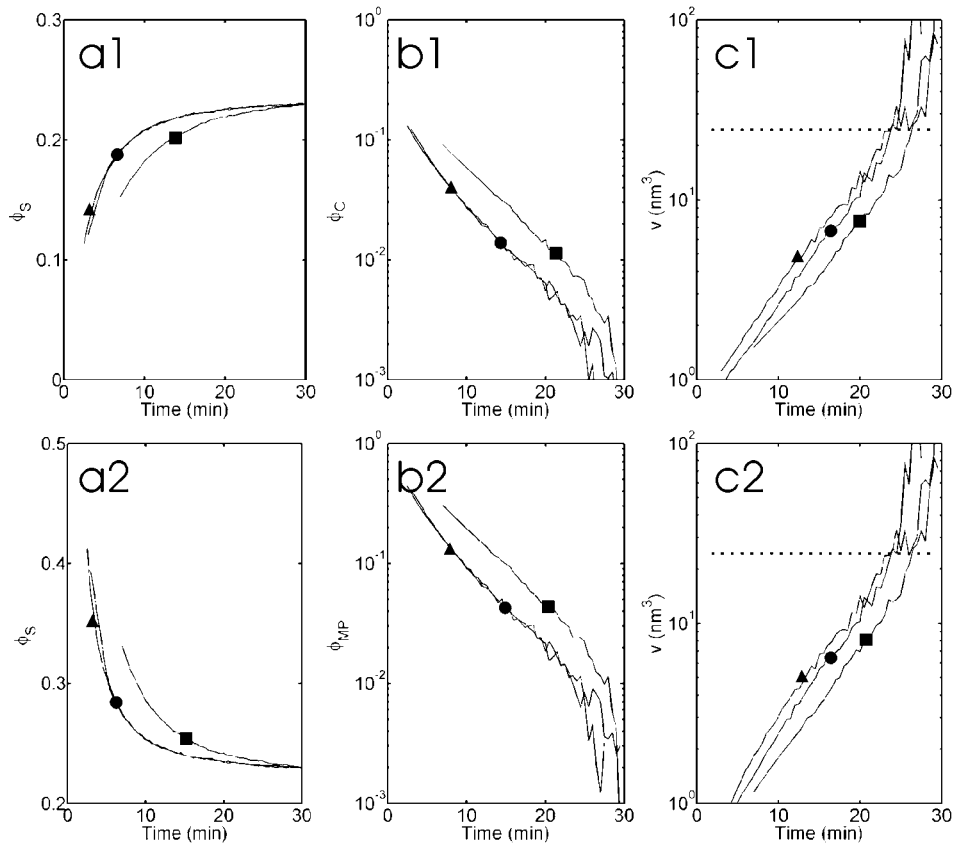


FIG. 7. Evolution of morphological parameters during the formation of the gels with  $R/C = 250$  (■),  $200$  (●), and  $150$  (▲). The top row is for model A: (a1) volume fraction of the skeleton  $\phi_S$ , (b1) volume fraction of the colloids  $\phi_C$  in the pores, (c1) volume of the colloids. The bottom row is for model B: (a2) volume fraction of the skeleton  $\phi_S$ , (b2) volume fraction of the micropores  $\phi_{MP}$  within the skeleton, (c2) volume of the micropores. The horizontal dotted line in (c1) and (c2) is roughly the resolution limit of the SAXS; the analysis is valid only for values of  $v$  below the line.

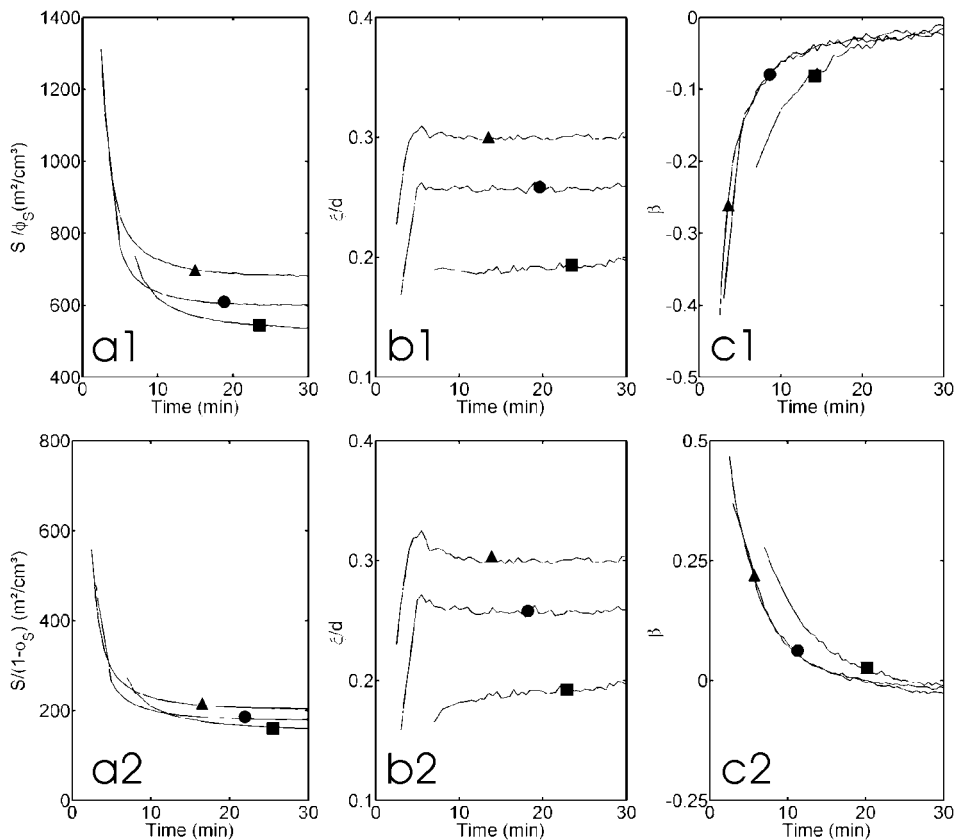


FIG. 8. Evolution of the skeleton's morphology during the formation of the gels with  $R/C = 250$  (■),  $200$  (●), and  $150$  (▲), for model A (top row) and model B (bottom row): (a) specific surface area  $S/\phi_S$  (model A) and  $S/(1-\phi_S)$  (model B), (b) ratio of the two characteristic lengths of the Gaussian random fields  $\xi/d$ , and (c) upper threshold  $\beta$  used to level-cut the Gaussian random fields.

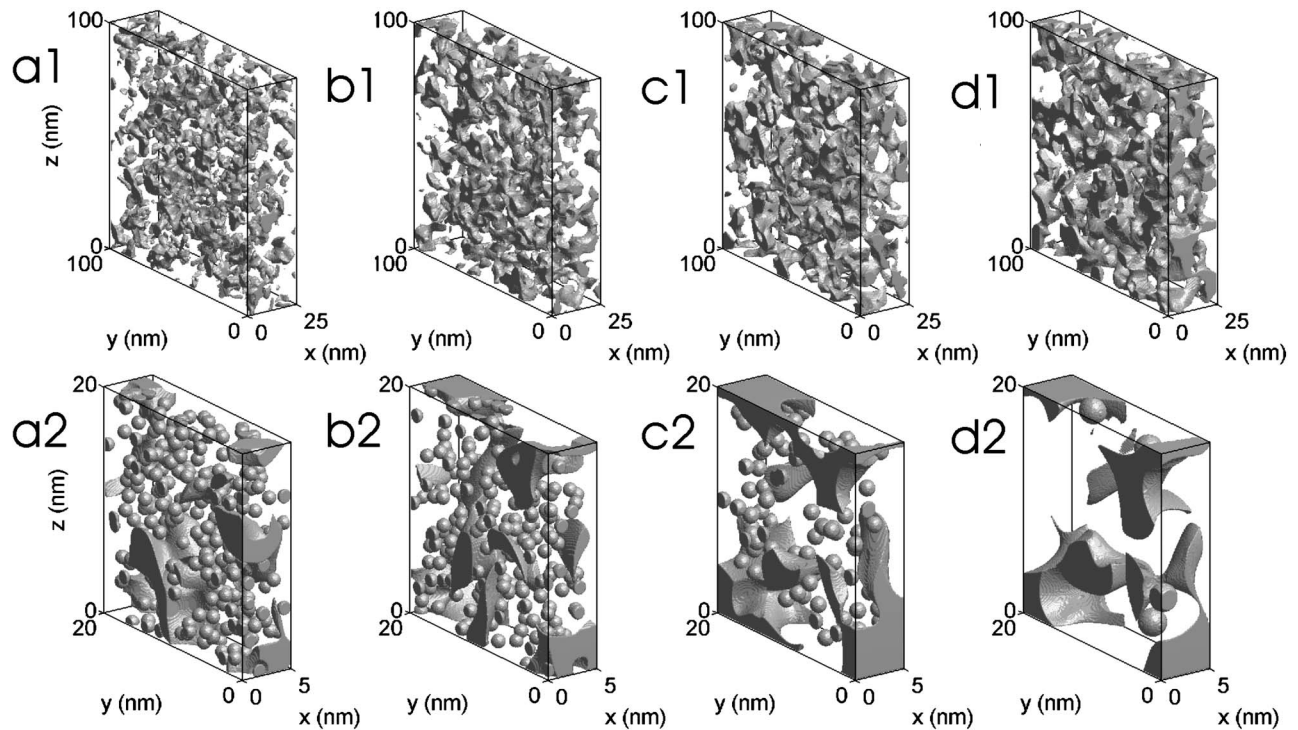


FIG. 9. Possible evolution of the morphology of the gel with  $R/C=150$  as a function of reaction time for  $t=2.5$  (a), 3.5 (b), 5 (c), and 20 min (d), according to model A [see Fig. 4(a)]. Top row, morphology of the skeleton, and bottom row, morphology of the colloidal suspension that fills the mesopores. The analysis gives no information about the shape of the colloids; they are represented as spheres for convenience.

vation of the total volume of polymer during the gel formation, and (ii) that the morphology has two different length scales, one of which falls in the SAXS range (roughly from 3 to 60 nm) and the other contributes to a uniform background scattering in the measured angular range. Two specific models are considered: in model A, the small-scale structure is a colloidal polymer suspension that fills the pores of the skeleton; in model B the small-scale structure consists of micropores within the gel's skeleton.

To analyze the morphology of the large-scale structure, the intersection model of Roberts is used [18]. That model was initially proposed to analyze resorcinol-formaldehyde aerogels. Aerogels are obtained from gels by supercritical solvent removal, and it is therefore expected that the morphologies of the solid skeleton of the gels and aerogels are identical (see, e.g., [2]). For the aerogels, the intersection model was validated not only for the SAXS—i.e., for two-point probability functions—but also for thermal conductivity which depends on higher-order statistics [18,23]. It is therefore believed that the model captures many morphological features of resorcinol-formaldehyde aerogels and gels. The fit of the SAXS of the final gels is quite satisfactory [Fig. 5(a)], and the different morphologies of the gels synthesized with various  $R/C$  ratios (Fig. 6) are also in agreement with the known morphology of the xerogels obtained after drying [19]. On the basis of microscopy and of nitrogen physisorption, synthesizing gels with a lower  $R/C$  ratio results in smaller structures and pores (see, e.g., [15]), in agreement with the present SAXS. Our analysis also shows that the structure becomes qualitatively more ordered, as as-

essed by the fact that  $\xi/d$  passes from *ca* 0.2 for  $R/C=250$  to 0.3 for  $R/C=50$ .

The time-dependent volume fraction of the skeleton and of the relevant small-scale structure (colloids or micropores) is determined from the value of Porod's invariant  $Q$ , and the volume of the colloids or micropores is determined from the background intensity  $I_0$ . The interpretation of the data plotted in Fig. 7 depends on the model used to analyze them. On one hand, in the framework of model A [Fig. 4(a)], the evolution of  $\phi_S$ ,  $\phi_C$ , and  $v$  is interpreted as a progressive increase of the volume of the skeleton at the expense of the colloidal suspension in its pores. Concomitantly, the volume of the colloids remaining in the pores increases, which is expected if they aggregate. The exponential growth [Figs. 7(b1) and 7(c1)] could also find an explanation in the context of a reaction-limited aggregation [29]. On the other hand, in the framework of model B [Fig. 4(b)], the skeleton of the gel is initially very voluminous and very porous; its volume fraction progressively decreases together with its porosity. In the context of gels, such a process is generally referred to as syneresis and it is common to phase separation [2,10]. The growth of the remaining micropores [Fig. 7(c2)] can also be understood because  $v$  is an average volume and the smallest pores are likely to be the first to disappear. In this context also the exponential kinetics of Figs. 7(b2) and 7(c2) is not surprising [30].

Figure 9 and 10 represent realizations of model A and B, respectively, in the course of the formation of the gel with  $R/C=150$ . The morphological parameters used result from the fit of the SAXS data in Fig. 5(b); they are plotted in Fig.

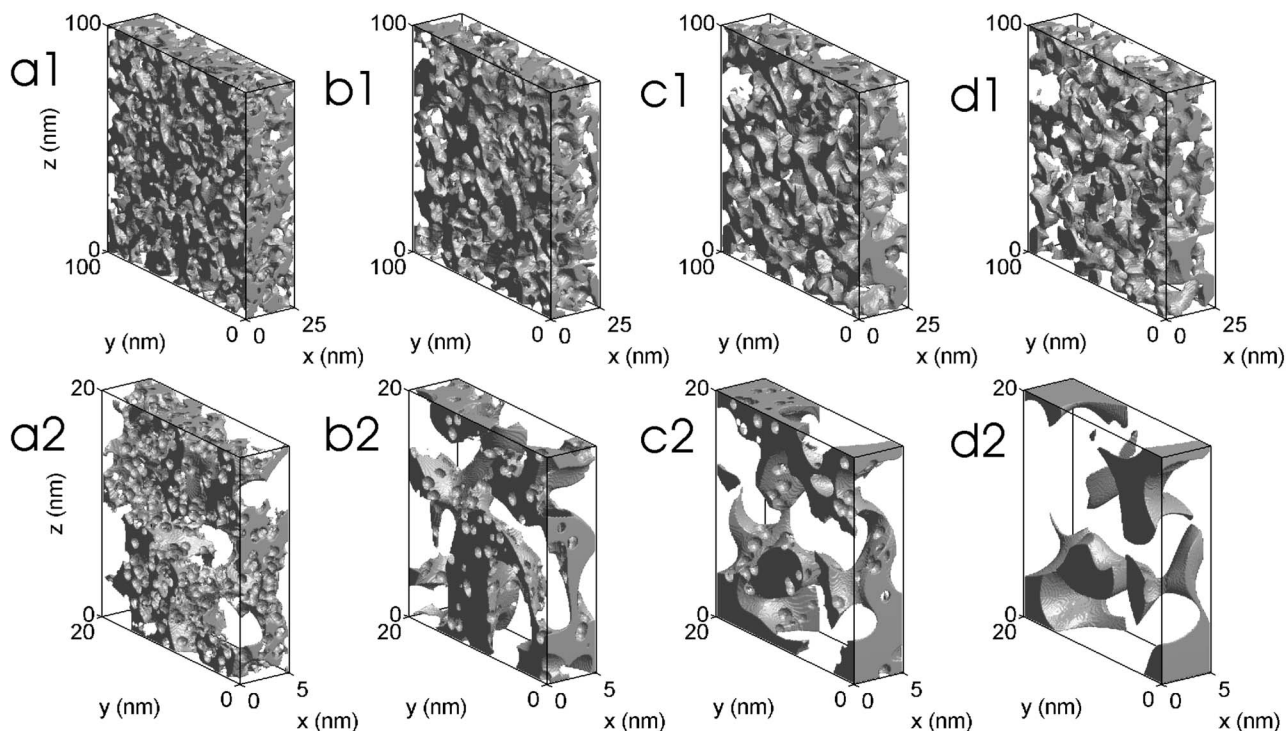


FIG. 10. Possible evolution of the morphology of the gel with  $R/C=150$  as a function of reaction time for  $t=2.5$  (a),  $3.5$  (b),  $5$  (c), and  $20$  (d), according to model B [see Fig. 4(b)]. Top row, morphology of the skeleton, and bottom row, small-scale morphology of the skeleton showing its microporosity. The analysis gives no information about the shape of the micropores; they are represented as spherical for convenience.

7 and 8. The small-scale structures are represented as spheres—spherical colloids in model A, and spherical micropores in model B—although the only information available is their average volume  $v$  and volume fraction  $\phi_C$  or  $\phi_{MP}$ . Although the final structure of the gels is the same for both models [Figs. 9(d1), 9(d2), 10(d1), and 10(d2)], they correspond to apparently very different reaction pathways.

The behavior of model A approximately corresponds to the aggregation theory of gel formation [3,31,32], which some authors use to analyze the formation of resorcinol-formaldehyde gels (see, e.g., [15]). This theory was popularized in the 1980s and 1990s, notably through the use of fractal concepts like diffusion-limited or reaction-limited aggregation [5,6]. According to this theory, the gels form via the formation of colloidal particles that aggregate until they form a space filling cluster, at which moment a gel is obtained. Quite often, the clusters take the form of filamentary aggregates of particles that are sometimes referred to as a string of pearls. The SAXS data of gels and aerogels can sometimes be modeled as aggregates of polydisperse colloidal particles [33]; the fits are very poor when polydispersity is not incorporated in the model [34]. The intersection model used in the present work exhibits a string-of-pearls morphology and its polydispersity can be tuned very naturally through the factor  $\xi/d$  (see the Appendix). At early reaction times, the skeleton is made of very small objects with a large specific surface area [Fig. 8(a1)], a large polydispersity as assessed by the low values of  $\xi/d$  [Fig. 8(b1)], and these objects do not form a percolating network as assessed by the initial low value of  $\beta$  [Fig. 8(c1)]. In the course of the gel

formation, the skeleton increases its volume [Fig. 7(a1)], it coarsens [Fig. 8(a1)], and becomes more ordered [Fig. 8(b1)] and better connected [Fig. 8(c1)].

On the other hand, the behavior of model B more closely mimics the microphase separation theory of gel formation (see, e.g., [12]), which some authors use to analyze the formation of resorcinol-formaldehyde gels [16]. According to this theory, the precursor molecules polymerize and form a branched network in which the polymer and the solvent are mixed at the molecular scale. When the degree of branching and/or the molecular weight increases, the solubility of the polymer in the solvent decreases which leads to syneresis [10]: the polymer chains progressively fold to form locally denser structures from which the solvent is expelled. The skeleton of the gel is initially very voluminous with  $\phi_S \sim 0.5$  [Figs. 7(a2) and 10(a1)], but it contains a large amount of solvent  $\phi_{MP} \sim 0.5$  [Figs. 7(b2) and 10(a2)] under the form of very small pores that are almost of molecular size [Fig. 7(c2)]. In the course of the gel structuring process, these pores progressively disappear, and the largest pores outside the skeleton increase in size, as indicated by the lowering of  $S/(1-\phi_S)$ . At the same time, the structure becomes more ordered [Fig. 8(b2)] as indicated by the appearance of a maximum in the SAXS patterns. Actually, the presence of a maximum in SAXS patterns of gels and aerogels is often considered as a proof for the occurrence of microphase separation (see, e.g., [16]), because microphase separation generally occurs on a well-defined length scale that depends on the degree of branching of the macromolecules [10].

Although aggregation and microphase separation seem to be two distinct processes, the present analysis shows that—in

the case of resorcinol-formaldehyde gels—both scenarios can lead to very similar morphologies. The fact that models A and B are both compatible with the SAXS data shows that the corresponding morphologies are not very different after all, as they have the same two-point probability functions above 3 nm. In principle, several different morphologies can have the same two-point probability function. In practice, however, a knowledge of the two-point function is often sufficient to reconstruct the corresponding morphology [25]. The similarity between the morphologies of models A and B above 3 nm is also seen from Figs. 9 and 10.

The physical difference between aggregation and phase separation should not be overestimated either. Although both scenarios are physically sound, none of them is fully satisfactory when it is considered alone. On one hand, the colloidal aggregation model predicts a fractal structure that is seldom observed experimentally over more than one decade of length scale [35]. Also, the aggregation model predicts a gel time that is dependent on the volume of the gel (see, e.g., [36]), in disagreement with experiment. A volume-independent gel time can be obtained if the aggregates are allowed to reorganize their inner structure as in the fluctuating bond model [37]. Furthermore, the latter reorganization of the aggregates—very similar to a microphase separation—is needed to account for the mechanical properties of the gels [38]. On the other hand, the pure microphase separation scenario is not fully satisfactory either. It is, for instance, well known that polycondensation leads to polymers with a broad molar mass distribution [2,39]: even after the gel time, most of the polymer is not connected to the percolating network. At the moment of the microphase separation, the pores of the incipient gel's skeleton are therefore necessarily filled with a suspension of colloidal polymer that can afterward aggregate. Therefore, colloidal aggregation and microphase separation should not be regarded as mutually exclusive mechanisms, but rather as two different idealizations of the same complex physical process.

## V. CONCLUSIONS

SAXS patterns of resorcinol-formaldehyde gels can be modeled with the intersection model initially proposed to model the SAXS and thermal conductivity of the resorcinol-formaldehyde aerogels. To analyze time-resolved SAXS data in the course of the gel formation, however, it is necessary to generalize the model in order to introduce a small-scale structure. This can be done in two different ways: it can be assumed that the mesopores of the skeleton are filled with a colloidal polymer suspension, or it can be assumed that the skeleton of the gel contains pores which are a few nanometers across. The two morphological models correspond to two apparently different mechanisms of gel formation, namely colloid aggregation and microphase separation. Both are compatible with the time-resolved SAXS data.

The fact that the two models can be used to fit the same data set points to the morphological similarity between realistic structures formed by colloidal aggregation and by microphase separation, in the length scales explored by the SAXS. Physical arguments also show that these two mecha-

nisms are not mutually exclusive and that they can be regarded as two idealizations of the same complex physical process.

## ACKNOWLEDGMENTS

C.J.G. acknowledges support from the Belgian national funds for scientific research (FNRS). The authors are grateful to Dr. Bart Goderis (Katholieke Universiteit Leuven) and to Dr. Florian Meneau (DUBBLE, European Synchrotron Radiation Facility), as well as to Dr. Nathalie Job and Dr. René Pirard (University of Liège) for their help during the measurement of the time-resolved SAXS data; fruitful discussion with Dr. Silvia Blacher (University of Liège) is also acknowledged. Part of this work was done during a stay of C.J.G. in Brisbane, supported by the University of Queensland and by the Patrimoine de l'Université de Liège.

## APPENDIX

A Gaussian random field  $y(\mathbf{x})$  can be constructed as a superposition of plane waves as

$$y(\mathbf{x}) = \sqrt{\frac{2}{N}} \sum_{i=1}^N \cos(\mathbf{k}_i \cdot \mathbf{x} - \phi_i), \quad (\text{A1})$$

where  $\mathbf{k}_i$  and  $\phi_i$  are independent random numbers;  $\phi_i$  is uniformly distributed in  $[0, 2\pi)$  and the probability distribution  $P(k)$  of the wave vectors  $\mathbf{k}_i$  is rotationally symmetric. When  $N$  is very large, the value of  $y(\mathbf{x})$  at any given  $\mathbf{x}$  is a Gaussian variable; the factor  $\sqrt{2/N}$  in Eq. (A1) ensures that its variance is 1 [40]. The GRF is completely determined by its two-point correlation function  $g(r) = \langle y(\mathbf{x} + \mathbf{r})y(\mathbf{x}) \rangle$  (where  $r = |\mathbf{r}|$ ), or equivalently by the probability density function of  $k = |\mathbf{k}|$  given by [40]

$$P(k) = \frac{2}{\pi} k \int_0^\infty r g(r) \sin(kr) dr. \quad (\text{A2})$$

In the last equation, the erroneous factor  $(2\pi)^3$  of Eq. (42) of Ref. [40] was replaced by  $2/\pi$ .

A useful description of porous media is provided by modeling the internal surface as an isosurface (or level cut) of a Gaussian random field  $y(\mathbf{x})$ . This approach has proved successful for the modeling the morphology of systems arising from spinodal decomposition [41], microemulsion [42,43], and polymer blends [44], among others [45]. For the level-cut model to have a finite specific surface area, the leading term in the Taylor development of  $g(r)$  has to be quadratic [40],

$$g(r) = 1 - (r/l)^2 + \dots \quad \text{for } r \rightarrow 0, \quad (\text{A3})$$

where  $l$  is a constant having the dimension of a length. If the condition of Eq. (A3) is not met, the level-cut morphology is a surface fractal with an infinite specific surface area. This is notably the case if the leading term in  $g(r)$  is linear as in an exponential, in which case the surface fractal dimension is 2.5 [40].

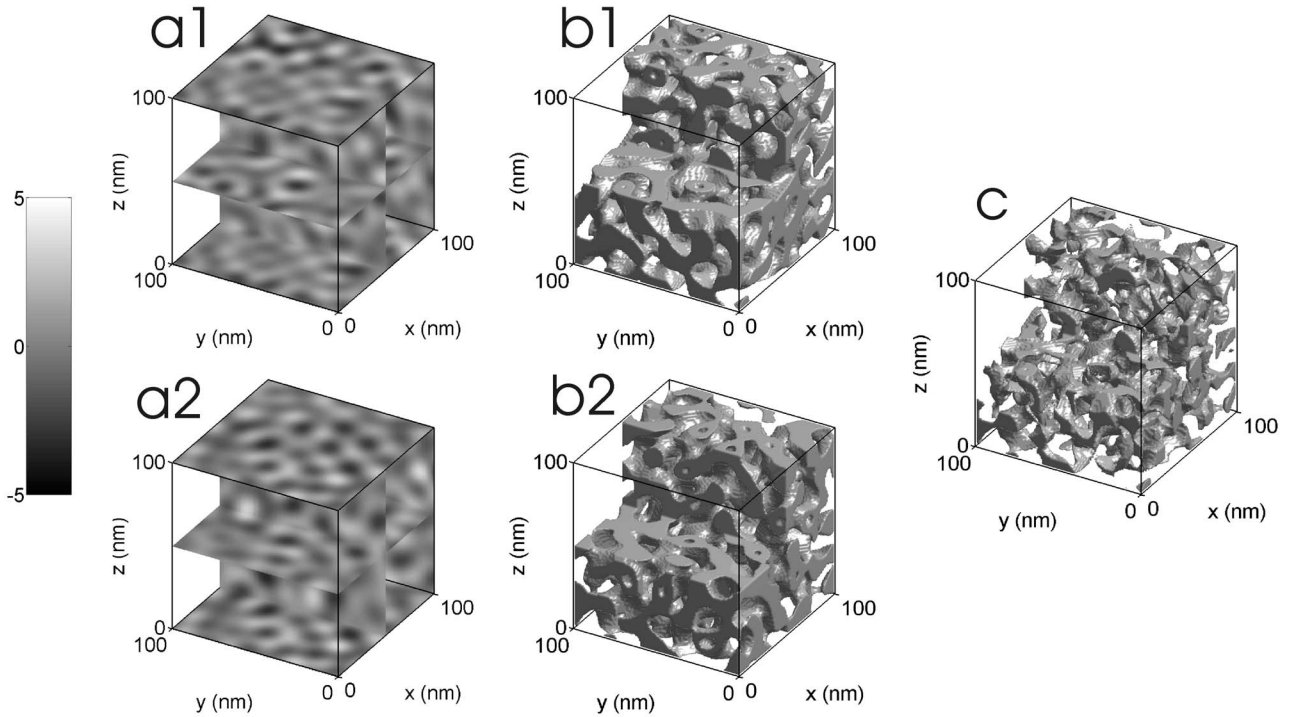


FIG. 11. Example of two independent realizations of a Gaussian random field  $y(\mathbf{x})$  with field-field correlation function given by Eq. (15) with  $d=60$  nm and  $\xi=20$  nm [(a1) and (a2)]; two-cut morphologies obtained by thresholding these random fields between  $\alpha=-2.3$  and  $\beta=0$  [(b1) and (b2)]; intersection of the two independent two-cut models (c).

Several analytical forms of  $g(r)$  satisfying Eq. (A3) have been used in the literature (see, e.g., [44,46]). The particular analytical form proposed in Eq. (15) of the main text satisfies Eq. (A3) with

$$\frac{1}{l^2} = \frac{2\pi^2}{3d^2} + \frac{1}{2\xi^2}. \quad (\text{A4})$$

Equation (15) has only two parameters  $d$  and  $\xi$ . The  $1/\cosh$  factor decreases asymptotically like an exponential function and the  $\sin(x)/x$  factor is needed to account for the presence of a maximum in the scattering patterns. In order to generate realizations of the GRF via Eq. (A1), it is necessary to calculate the wave vector probability density function: substituting Eq. (15) into Eq. (A2), one finds

$$P(k) = \frac{k}{\pi} \xi d \frac{\sinh(\pi k \xi / 2) \sinh(\pi^2 \xi / d)}{\cosh(\pi k \xi) + \cosh(2\pi^2 \xi / d)}. \quad (\text{A5})$$

Figures 11(a1) and 11(a2) represent two independent realizations of GRFs obtained by summing 500 plane waves according to Eq. (A1), with a wave vector probability distribution given by Eq. (A5) with  $d=60$  nm and  $\xi=20$  nm.

The simplest level-cut model consists in modeling the morphology of a given phase as the set of all points at which the GRF  $y(\mathbf{x})$  is lower than a given threshold [41]. Berk [42] generalized this model by introducing two thresholds  $\alpha$  and  $\beta$  and by defining, say, phase 1 to occupy the region of space where  $\alpha \leq y(\mathbf{x}) \leq \beta$ , and phase 2 to occupy the remainder. As the values of  $y(\mathbf{x})$  are Gaussian distributed with a variance equal to 1, the volume fraction  $\phi_1$  of phase 1 is related to the thresholds via  $\phi_1 = p_\beta - p_\alpha$ , with [42]

$$p_\alpha = \frac{1}{\sqrt{2\pi}} \int_{-\infty}^{\alpha} \exp\left(-\frac{t^2}{2}\right) dt. \quad (\text{A6})$$

Figures 11(b1) and 11(b2) represent two independent realizations of two-cut morphologies with  $\alpha=-2.3$  and  $\beta=0$ .

The scattering properties of an isotropic system depend only on the two-point probability function  $P_{11}(r)$ , defined as the probability that two points chosen randomly in space and at a distance  $r$  from one another both belong to phase 1 (see, e.g., [23]). The two-point probability function is related to the field-field correlation function of the GRF and to the two thresholds via [47]

$$P_{11}(r) = \phi_1^2 + \frac{1}{2\pi} \int_0^{g(r)} \frac{dt}{\sqrt{1-t^2}} \left[ \exp\left(-\frac{\alpha^2}{1+t}\right) - 2 \exp\left(-\frac{\alpha^2 - 2\alpha\beta + \beta^2}{2(1-t^2)}\right) + \exp\left(-\frac{\beta^2}{1+t}\right) \right]. \quad (\text{A7})$$

The latter expression could be used in Eq. (10) of the main text to estimate the intensity scattered by the skeleton.

Models based on a single GRF, with either one or two cuts, are not useful to model the morphology of gels or aerogels. At densities typical of the latter systems, one-cut models consist of disconnected blobs corresponding to the regions of space where the GRF has its lowest values; the blobs become connected only at densities larger than about 15% [18]. On the other hand, two-cut models are connected at smaller densities. The latter models, however, have a shee-

tlike morphology that is not representative of the struts that constitute the skeleton of gels. Such sheets are visible from Figs. 11(b1) and 11(b2), in which it is seen that the solid phase is indeed hollow. To avoid the presence of these hollow structures, Roberts [18] proposed a model generated from the intersection of two statistically independent two-cut models [Fig. 11(c)]. The intersection of two structures with sheet morphology yields a structure with a strut morphology that can be used as a model of gels and aerogels. The statistical independence of the two intersected models enables the properties of the intersection to be calculated. In particular, the density of the intersection is related to the threshold via

$$\phi_1^I = (\phi_1)^2 = (p_\beta - p_\alpha)^2, \quad (\text{A8})$$

where  $p_\alpha$  and  $p_\beta$  are given by Eq. (A6). The two-point probability function of the intersection model  $P_{11}^I(r)$  is obtained as

$$P_{11}^I(r) = [P_{11}(r)]^2, \quad (\text{A9})$$

where  $P_{11}(r)$  is given by Eq. (A7). Using Eq. (A9) the scattered intensity can be estimated via Eq. (10) of the main text.

The specific surface area  $S/V$  of the intersection model can be calculated using the general relation [23,28]

$$\frac{S}{V} = -4 \left( \frac{dP_{11}(r)}{dr} \right)_{r=0}. \quad (\text{A10})$$

Using Eqs. (A10), (A9), and (A7) and the general relation Eq. (A3), the specific surface area of the intersection model is found to be

$$\left( \frac{S}{V} \right)^I = \frac{4}{\pi} \sqrt{2} \phi_1^I \left[ \exp\left( \frac{-\alpha^2}{2} \right) + \exp\left( \frac{-\beta^2}{2} \right) \right] \frac{1}{l} \quad (\text{A11})$$

with  $\phi_1^I$  given by Eq. (A8). In the particular case where Eq. (15) is used for the field-field correlation function,  $l$  is given by Eq. (A4); the specific surface area of the intersection model becomes

$$\left( \frac{S}{V} \right)^I = \frac{4}{\pi} \sqrt{2} \phi_1^I \left[ \exp\left( \frac{-\alpha^2}{2} \right) + \exp\left( \frac{-\beta^2}{2} \right) \right] \sqrt{\frac{4\pi^2}{6d^2} + \frac{1}{2\xi^2}}. \quad (\text{A12})$$

To illustrate the various morphologies that can be obtained through the intersection model, four realizations are represented in Fig. 12, obtained with the field-field correlation

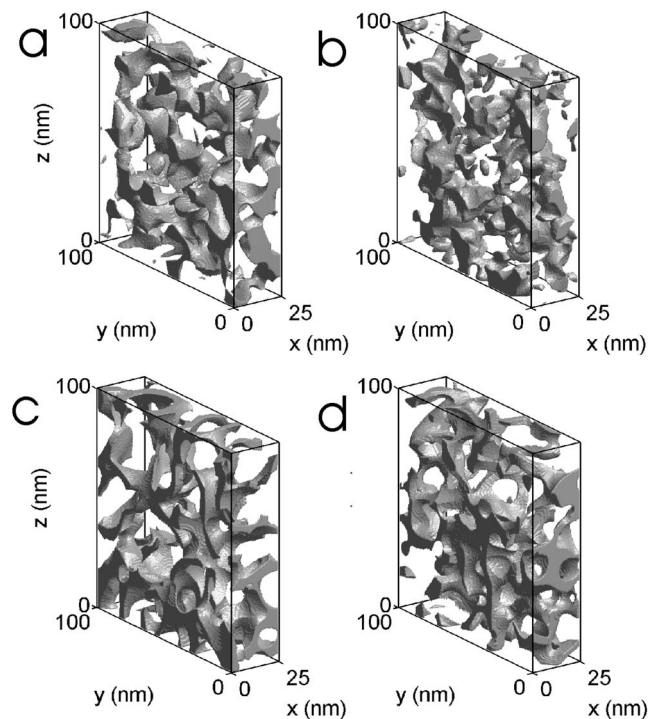


FIG. 12. Realizations of the intersection model with specific surface area of  $S=1000 \text{ m}^2/\text{cm}^3$  and volume fraction  $\phi=0.2$ : (a)  $\xi/d=0.5$  and  $\alpha=-\infty$ , (b)  $\xi/d=0.1$  and  $\alpha=-\infty$ , (c)  $\xi/d=0.5$  and  $\alpha=-\beta$ , (d)  $\xi/d=0.1$  and  $\alpha=-\beta$ .

given by Eq. (15) of the main text. All realizations in the figure correspond to a specific surface area of  $1000 \text{ m}^2/\text{cm}^3$  according to Eq. (A12), and a volume fraction  $\phi=0.2$  according to Eq. (A8). They differ in the ratio  $\xi/d$  and in the way in which the thresholds  $\alpha$  and  $\beta$  are chosen. Figures 12(a) and 12(b) are obtained with  $\alpha=-\infty$ ; they therefore correspond to a single cut; they have a continuous structure with local bulges, which has been described as a string-of-pearls morphology (see, e.g., [16]). Figures 12(c) and 12(d) on the other hand are obtained with  $\alpha=-\beta$ ; they have a fiber morphology. In both cases (string of pearls or fiber) decreasing  $\xi/d$  results in a more random or disordered structure. Increasing  $\beta$  at a given density results in a better connected structure.

[1] Y. Osada and J.-P. Gong, *Adv. Mater.* **10**, 827 (1998).  
 [2] C. J. Brinker and G. W. Scherer, *Sol-Gel Science: The Physics and Chemistry of Sol-Gel Processing* (Academic Press, San Diego, 1990).  
 [3] R. K. Iler, *The Chemistry of Silica: Solubility, Polymerization, Colloid and Surface Properties, and Biochemistry* (Wiley, New York, 1979).  
 [4] S. Lebon, J. Marignan, and J. Appel, *J. Non-Cryst. Solids* **147-148**, 92 (1992).  
 [5] A. Lecomte, A. Dauge, and P. Lenormand, *J. Appl. Crystal-*

*logr.* **33**, 496 (2000).  
 [6] P. Meakin, *Phys. Rev. Lett.* **51**, 1119 (1983).  
 [7] T. Viscek, *Fractal Growth Phenomena*, 2nd ed. (World Scientific, Singapore, 1992).  
 [8] D. W. Schaefer and K. D. Keefer, *Phys. Rev. Lett.* **53**, 1383 (1984).  
 [9] D. R. Vollet, D. A. Donatti, and A. Ibanez Ruiz, *J. Non-Cryst. Solids* **81**, 288 (2001).  
 [10] P.-G. de Gennes, *Scaling Concepts in Polymer Physics* (Cornell University Press, Ithaca, NY, 1979).

- [11] V. I. Raman and G. R. Palmese, *Langmuir* **21**, 1539 (2005).
- [12] A. Serrano Aroca, M. Monleón Pradas, and J. L. Gómez Ribelles, *Colloid Polym. Sci.* **285**, 753 (2007).
- [13] H. Tanaka, *Phys. Rev. Lett.* **76**, 787 (1996).
- [14] R. W. Pekala, *J. Mater. Sci.* **24**, 3221 (1989).
- [15] S. A. Al-Muhtaseb and J. A. Ritter, *Adv. Mater. (Weinheim, Ger.)* **15**, 101 (2003).
- [16] R. W. Pekala and D. W. Schaefer, *Macromolecules* **26**, 5487 (1993); D. W. Schaefer, R. Pekala, and G. Beaucage, *J. Non-Cryst. Solids* **186**, 159 (1995).
- [17] T. Yamamoto, T. Nishimura, T. Suzuki, and H. Tamon, *J. Non-Cryst. Solids* **288**, 46 (2001).
- [18] A. P. Roberts, *Phys. Rev. E* **55**, R1286 (1997).
- [19] N. Job, R. Pirard, J. Marien, and J.-P. Pirard, *Carbon* **42**, 619 (2004).
- [20] O. Glatter and K. Kratky, *Small-Angle X-ray Scattering* (Academic, London, 1982).
- [21] S. Ciccariello, J. Goodisman, and H. Brumberger, *J. Appl. Crystallogr.* **21**, 117 (1988).
- [22] J. Rouquerol, D. Avnir, C. W. Fairbridge, D. H. Everett, J. H. Haynes, N. Pernicone, J. D. F. Ramsay, K. S. W. Sing, and K. K. Unger, *Pure Appl. Chem.* **66**, 1739 (1994).
- [23] S. Torquato, *Random Heterogeneous Materials: Microstructure and Macroscopic Properties* (Springer, New York, 2001).
- [24] S. Ciccariello, *Phys. Rev. B* **28**, 4301 (1983).
- [25] Y. Jiao, F. H. Stillinger, and S. Torquato, *Phys. Rev. E* **76**, 031110 (2007).
- [26] J. S. Pedersen, *Adv. Colloid Interface Sci.* **70**, 171 (1997).
- [27] J. Serra, *Image Analysis and Mathematical Morphology* (Academic, Orlando, FL, 1983).
- [28] J. Ohser and F. Mücklich, *Statistical Analysis of Microstructures in Materials Science* (Wiley, Chichester, U.K., 2000).
- [29] M.Y. Lin, H.M. Lindsay, D.A. Weitz, R.C. Ball, R. Klein and P. Meakin, *Proc. R. Soc. London, Ser. A* **423**, 71 (1989).
- [30] B. Mohanty and H. B. Bohidar, *Europhys. Lett.* **76**, 965 (2006).
- [31] T. P. M. Beelen, W. H. Dokter, H. F. Van Garderen, and R. A. Van Santen, *Adv. Colloid Interface Sci.* **50**, 23 (1994).
- [32] A. Hasmy and R. Jullien, *J. Non-Cryst. Solids* **186**, 342 (1995).
- [33] D. Posselt, J. S. Pedersen, and K. Mortensen, *J. Non-Cryst. Solids* **145**, 128 (1992).
- [34] C. J. Gommès, S. Blacher, B. Goderis, R. Pirard, B. Heinrichs, C. Alié, and J.-P. Pirard, *J. Phys. Chem. B* **108**, 8983 (2004).
- [35] O. Malcai, D. A. Lidar, O. Biham, and D. Avnir, *Phys. Rev. E* **56**, 2817 (1997).
- [36] M. Kolb and H. J. Herrmann, *J. Phys. A* **18**, L435 (1985).
- [37] R. Jullien and A. Hasmy, *Phys. Rev. Lett.* **74**, 4003 (1995).
- [38] H.-S. Ma, R. Jullien, and G. W. Scherer, *Phys. Rev. E* **65**, 041403 (2002).
- [39] F. W. Billmeyer, *Textbook of Polymer Science*, 3rd ed. (Wiley-Interscience, New York, 1984).
- [40] N. F. Berk, *Phys. Rev. A* **44**, 5069 (1991).
- [41] J. W. Cahn, *J. Chem. Phys.* **42**, 93 (1965).
- [42] N. F. Berk, *Phys. Rev. Lett.* **58**, 2718 (1987).
- [43] M. Teubner, *Europhys. Lett.* **14**, 403 (1991).
- [44] H. Jinnai, T. Hashimoto, D. Lee, and S.-H. Chen, *Macromolecules* **30**, 130 (1997).
- [45] P. Levitz, *Adv. Colloid Interface Sci.* **76-77**, 71 (1998).
- [46] A. P. Roberts and M. A. Knackstedt, *Phys. Rev. E* **54**, 2313 (1996).
- [47] A. P. Roberts and M. Teubner, *Phys. Rev. E* **51**, 4141 (1995).